Journal of Solid State Chemistry 181 (2008) 1249–1257

Contents lists available at ScienceDirect

Journal of Solid State Chemistry

journal homepage: www.elsevier.com/locate/jssc

Shape controlled synthesis of $CaMoO_4$ thin films and their photoluminescence property

Ana Paula de Azevedo Marques [a,*], Valeria M. Longo [a], Dulce M.A. de Melo [b], Paulo S. Pizani [c], Edson R. Leite [a], José Arana Varela [d], Elson Longo [a,d]

[a] Laboratório Interdisciplinar de Eletroquímica e Cerâmica, Departamento de Química, Centro Multidisciplinar de Desenvolvimento de Materiais Cerâmicos, Universidade Federal de São Carlos, C. Postal 676, 13565-905 São Carlos, SP, Brazil
[b] Laboratório de Análise Térmica e Materiais, Departamento de Química, Universidade Federal do Rio Grande do Norte, 59072-970 Natal, RN, Brazil
[c] Laboratório de Semicondutores, Departamento de Física, Universidade Federal de São Carlos, C. Postal 676, 13565-905 São Carlos, SP, Brazil
[d] CMDMC, LIEC, Instituto de Química, Universidade Estadual Paulista, 14801-907 Araraquara, SP, Brazil

ARTICLE INFO

Article history:
Received 7 December 2007
Received in revised form
29 January 2008
Accepted 30 January 2008
Available online 2 March 2008

Keywords:
$CaMoO_4$
Photoluminescence
Thin films
Complex polymerization method
Ordered–disordered
ab initio calculations

ABSTRACT

$CaMoO_4$ (CMO) disordered and ordered thin films were prepared by the complex polymerization method (CPM). The films were annealed at different temperatures and time in a conventional resistive furnace (RF) and in a microwave (MW) oven. The microstructure and surface morphology of the structure were monitored by atomic force microscopy (AFM) and high-resolution scanning electron microscopy (HRSEM). Order and disorder were characterized by X-ray diffraction (XRD) and optical reflectance. A strong photoluminescence (PL) emission was observed in the disordered thin films and was attributed to complex cluster vacancies. The experimental results were compared with density functional and Hartree–Fock calculations.

1. Introduction

Materials belonging to the molybdate and tungstate families have a long history of practical applications and have been the object of extensive research over the past century. The continuing interest in these compounds lies in their excellent optical properties, which form the basis of their wide use as phosphors, laser materials, and scintillation detectors [1,2].

$CaMoO_4$ (CMO) has a scheelite-type crystalline structure (tetragonal symmetry C_{4h}^6). This structure attracts great attention due to its property of producing green luminescence. Because of the wide variety of technical applications of CMO thin films in electronics, optics, ionics and anticorrosion coatings, much interest has focused on their preparation [3–7].

CMO powders with a scheelite structure have been synthesized by a variety of techniques, including combustion synthesis [8], the Chochralski technique [9], conventional solid-state reaction [10] and the complex polymerization method (CPM) [5]. However, references in the literature about the synthesis of CMO thin films are rare and most commonly cited method is the electrochemical route [6,11]. Barium molybdate thin films obtained by the electrochemical method showed heterogeneous surfaces and grains with sizes varying from 2 to 10 μm [7,12]. However, $BaMoO_4$ thin films prepared by the CPM presented homogeneous surfaces and grain sizes ranging from 280 to 320 nm [4]. When the CPM is used, the metal-complexes become immobilized in a rigid organic polymeric network, reducing the segregation of particular metals and thus ensuring compositional homogeneity on a molecular scale [4,5,13].

Crystalline molybdates are compounds with strong natural green photoluminescence (PL) at room temperature and are interesting materials for technological applications, including solid-state optoelectronic devices. They are structurally similar to tungstates and the PL spectra presented by these materials can often be broken down into green, yellow and red contributions. However, the interpretation of the PL spectra of molybdates and tungstates, mainly insofar as the green contribution is concerned, is still a matter of controversy. Groenink and Blasse [14] and Korzhik et al. [15–17] concluded that green emission originates from the (WO_3+F) center. Sokolenko et al. [18] attributed green-red emission to WO_3, $V_O^{\cdot}$ oxygen-deficient complexes. Sinelnikov et al. [19] suggested that WO_4 tetrahedra which become distorted

* Corresponding author. Fax: +55 16 3351 8214.
E-mail addresses: apamarques@liec.ufscar.br, apamarques@hotmail.com (A.P.A. Marques).

0022-4596/$ - see front matter © 2008 Elsevier Inc. All rights reserved.
doi:10.1016/j.jssc.2008.01.051

upon the formation of oxygen vacancies are responsible for the green luminescence band. In addition, several authors [20–23] attribute the green PL component to defect centers with oxygen interstices.

Using time-resolved spectroscopy, Leonelli and Brebner proposed a model to describe the luminescence process whereby electrons form small polarons that interact with holes to produce self-trapped excitons (STEs), with the recombination of STEs resulting in the visible emission, either immediately or after being trapped for a certain time by impurities and defects [24,25].

More recently, several PL phenomena at low temperatures have been reported for the perovskite-type structure and the effects observed have been linked to the recombination of electrons and hole polarons, forming a charge transfer vibronic exciton (CTVE) [26,27].

Our group recently demonstrated that a series of ABO_4 scheelite-type structures, where $A = Sr$, Ca or Ba and $B = W$ or Mo, synthesized by the CPM, displayed intense visible PL at room temperature when the structure was not completely ordered [4,28,29].

From the experimental standpoint of this work, a number of complementary characterization techniques were used, such as X-ray diffraction (XRD), optical reflectance, Fourier transform infrared reflectance spectra (FTIR) and photoluminescence (PL) spectroscopy, to obtain a clearer picture of the physics underlying the luminescence behavior of the ordered and disordered CMO scheelite structure. Using a theoretical approach to the experimental PL results of green, yellow and red light emission, three types of disorder were simulated in the network former (Mo atom) of the crystalline (ordered) tetragonal unit cell. These theoretical simulations enabled to demonstrate how different intrinsic defects contribute to the disordered system and give rise to specific states in the forbidden gap, leading to different electronic transitions and, hence, to light emissions of different colors.

2. Experimental procedure

2.1. Preparation of CMO thin films

CMO thin films were produced by deposition of the polymeric resin obtained by the CPM onto Si substrates. In this synthesis, the molybdenum citrate was formed by the dissolution of molybdic acid (MoO_3—molybdenum trioxide) in an aqueous solution of citric acid under constant stirring at 60–80 °C to homogenize the molybdenum citrate solution (the molar ratio of citric acid to molybdic acid was 6:1). After this solution was homogeneized, a stoichiometric amount of calcium carbonate was added and dissolved in the molybdenum citrate solution. The complex was stirred thoroughly for several hours at 60–80 °C to produce a clear and homogeneous solution. Ethylene glycol was then added to promote polymerization of the citrate by polyesterification. The viscosity of the solution increased under continual heating at 80–90 °C, although no phase separation was visible. The molar ratio of calcium to molybdenum cations was 1:1. The citric acid/ethylene glycol mass ratio was set at 60:40. The viscosity of the deposition solution was adjusted to 15 mPa/s by controlling the water content.

A total of six thin films were produced using Si wafers as substrates. The substrates were spin-coated by dropping a small amount of the polymeric resin onto them. Rotation speed and spin time were fixed at 700 rpm for 3 s and 7200 rpm for 30 s, using a commercial spinner (Chemat Technology KW-4B spin-coater). After deposition, the films were heat-treated at 80 °C for 30 min, 100 °C for 20 min and 200 °C for different lengths of time (2, 4, 8 or 16 h), applying a heating rate of 1 °C/min. Four layers were deposited and the procedure was repeated for each layer. In the last layer, after the heat treatment at 200 °C, the crystallization procedure was applied to two thin films, one of which was heat-treated at 600 °C for 2 h in a resistive furnace (RF) and the other at 600 °C for 10 min in a microwave (MW) oven. The heat treatments applied in the films, after the heat treatment at 80 and 100 °C, are described in Table 1.

Table 1
Heat treatments applied in the $CaMoO_4$ thin films after heat treatment at 80 and 100 °C

Sample code	Time (h)	Temperature (°C)
CMO-2	2	200
CMO-4	4	200
CMO-8	8	200
CMO-16	16	200
CMO-RF	2	200
	2	600
CMO-MW	2	200
	0.17 (10 min)	600

CMO thin films were characterized by XRD using Cu$K\alpha$ radiation to determine the resulting phases. The optical reflectance was measured in the wavelength range of 200–800 nm, using a UV–Vis–NIR Cary 5 G spectrophotometer. FTIR for thin films were recorded in the frequency range of 400–2100 cm^{-1} at room temperature, using an Equinox/55 (Bruker) spectrometer equipped with a 30° specular reflectance accessory. Atomic force microscopy (AFM) was used to obtain and reconstruct a 3D image of the surface of the sample. These images allow for accurate analysis and quantification of highly relevant parameters such as roughness and grain size. A digital instruments multi-mode nanoscope IIIa microscope was used. The microstructure and surface morphology of the thin films were observed by high-resolution scanning electron microscopy (HRSEM) using a field emission gun (Gemini-Zeiss Supra35). PL spectra of CMO thin films were recorded with a U1000 Jobin-Yvon double monochromator coupled to a cooled GaAs photomultiplier and a conventional photon counting system. The 488.0 nm exciting wavelength of an argon ion laser was used. The maximum output power of the laser was 20 mW. All the measurements were taken at room temperature.

2.2. Periodic models

Scheelite CMO crystallizes in a tetragonal structure (space group $I4_1/a$, $C_{4h}{}^6$ symmetry). Molybdenum atoms are surrounded by four oxygen atoms in a tetrahedral configuration and calcium atoms are surrounded by eight oxygens in a pseudo cubic configuration. A single primitive cell was used as a periodic model to represent the ordered CMO-o. This model can be designed as $[MoO_4]$–$[MoO_4]$, since each molybdenum atom is surrounded by four oxygen atoms in a $C_{4h}{}^6$ configuration. This results in 12 atoms in the unit cell presented in Fig. 1(a). The ordered and disordered structures ($a = 5.2259$ Å and $c = 11.4419$ Å) were calculated based on the experimental values of a Rietveld analysis.

Experimental X-ray absorption near edge structure (XANES) results [30] of the disordered phase of ST revealed the coexistence of two types of environments for the titanium, namely, five-fold titanium coordination $[TiO_5 \cdot V_O^Z]$, $V_O^Z = V_O^X$, $V_O^{\cdot}$, $V_O^{\cdot\cdot}$ and six-fold titanium coordination $[TiO_6]$. Based on this information, it was assumed that before the films become completely crystallized, the structure is composed of an aleatory mixture of $[MoO_4]$ and $[MoO_3 \cdot V_O^Z]$ complex clusters linked by the Ca. Three unit cells were therefore created to stand for the disordered models (CMO-d).

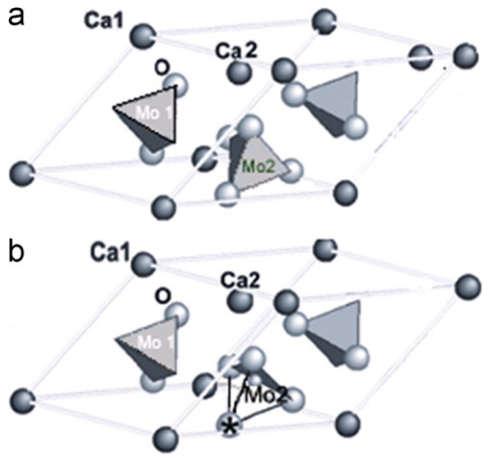

Fig. 1. (a) CMO-o periodic model: $1 \cdot 1 \cdot 1$ cell of the $CaMoO_4$ primitive unit cell. (b) CMO-d periodic model: Mo2 was shifted by 0.3 Å.

Starting from the previous CMO-o model, the Mo2 atoms were shifted from 0.1, 0.2 and 0.3 Å in the direction opposite that of the starred oxygens of Fig. 1(b), thereby breaking the bonds. Because of their asymmetry, these new disordered periodic models are called CMO-d_1 (0.1 Å), CMO-d_2 (0.2 Å) and CMO-d_3 (0.3 Å). The Mo2 atoms are now surrounded by three oxygen atoms in this first coordination sphere.

These four models can describe the continuous behavior of the order in CMO-o and introduce disordered discontinuities in disordered CMO-d; each of the $[MoO_4]$ complex clusters is accompanied by a distortion that leads to $[MoO_3 \cdot V_O^Z]$, where $V_O^Z = V_O^X, V_O^{\cdot}, V_O^{\cdot\cdot}$.

Using the CRYSTAL98 package [31], calculations were carried out based on both the density functional (DFT) and Hartree–Fock theories. The gradient-corrected correlation functional by Lee et al. was used, combined with the Becke3 exchange functional, B3LYP [32,33], which was demonstrated by Muscat et al. [34] to be suitable for calculating structural parameters and band structures for a wide variety of solid-state compounds. The basic sets used for the atomic centers were Mo [35], Ca (86-511d3G) [24] and O (6-31G*) [36]. To simulate the displacement of the Mo2 atoms (as defined in Fig. 1b), we used the ATOMDISP (atoms displacement) option of the CRYSTAL program. *K*-points sampling was chosen as 36 points within the irreducible part of the Brillouin zone. The XcrysDen program was used to design the density of states and band structure diagrams [37].

Our aim with this modeling was not to represent the exact reality of the disordered structures, but to offer a simple scheme allowing one to understand the effects of structural deformation on the electronic structure without completely suppressing the geometry of the cell, which is useful for the periodic calculation. These models can be useful to represent different degrees of order–disorder in matter and structural intrinsic defects that derive from the presence of $[MoO_4]$ and $[MoO_3 \cdot V_O^X]$ complex clusters.

3. Results and discussion

Figs. 2 and 3a show X-ray patterns of CMO thin films deposited onto Si substrates after heat treatments in the RF and MW oven at 200 and 600 °C for various lengths of time. The diffraction peak (112) (100% peak) occurred in the same 2θ region of Si substrate, 2θ around of 28.8°; hence, there was overlapping. However, other peaks corresponding to the crystalline CMO scheelite-type phase were visible in both ordered thin films heat-treated at 600 °C (Fig. 3a). The diffraction peaks were indexed according to the JCPDS data base no. 29-0351 [38]. The thin film heat-treated by MW showed two additional peaks in the 2θ region around 36° and 48°, which corresponded to the CaO deleterious phase [39]. Fig. 2a does not show the diffraction peak corresponding to the CMO phase (112), indicating that the thin films heat-treated at 200 °C between 2 and 16 h were disordered and devoid of crystallized phases. The intensity of substrate peaks changes according to the thickness of thin films: thicker thin films display lower substrate peaks than do thinner thin films [4]. The lattice parameters were calculated using a least-squares refinement REDE93 program, which yielded values of $a = 5.223(11)$ Å and $c = 11.397(36)$ Å for the thin film heat-treated in the RF and $a = 5.219(2)$ Å and $c = 11.422(6)$ Å for the film heat-treated in the MW oven. These values are in good agreement with those corresponding to the structure of the bulk material [38]. The experimental Rietveld analysis values of the *a* and *c* parameters were 5.2259 and 11.4419 Å, respectively (used for the *ab initio* calculations). The cell volume of ordered CMO thin films heat-treated, respectively, in the RF and MW, were 310.91 and 311.11 $Å^3$. These values are highly congruent with others reported in the literature (312.17 $Å^3$) [38].

The representation of the tetrahedral symmetry is $\Gamma_{Td} = A_1(v_1) + E(v_2) + F_2(v_3) + F_2(v_4)$, but only the $F_2(v_3, v_4)$ modes are IR active. The $F_2(v_3)$ vibrations are antisymmetric stretches, whereas the $F_2(v_4)$ vibrations are bending modes. The FTIR absorption spectrum of ordered CMO thin films presented an intense band at around 797 cm^{-1}. This band has been assigned to $F_2(v_3)$ antisymmetric stretching vibrations, corresponding to the Mo–O stretching vibration in the MoO_4^{2-} tetrahedron [4,5,40]. The disordered CMO thin films did not present $F_2(v_3)$ vibrations, in line with the XRD data.

A detailed AFM analysis revealed differences in terms of surface morphology for CMO thin films heat-treated at 200 and 600 °C (Figs. 2 and 3b, respectively). The AFM analyses clearly indicated that all the disordered CMO thin films heat-treated at 200 °C had a homogeneous surface morphology with very low roughness (between 2.2 and 3.2 nm). There was no evidence of granular structures. Conversely, the surface morphology significantly changed upon heat treatment at 600 °C. At this stage, nuclei coalescence took place, accompanied by the formation of a granular structure, thus increasing the roughness of the film (349 nm). This result was in good agreement with XRD data, which revealed significant crystallization after the heat treatment at 600 °C. The AFM analysis showed that the crystalline thin films presented homogeneous nucleation, resulting in grain sizes of around 170 nm, in line with the characteristics revealed in the HRSEM micrographs (Fig. 3b–d).

Figs. 3c and d depict cross-section and surface HRSEM micrographs of the CMO thin films. The CMO thin film MW-treated at 600 °C for 10 min had a thickness of 107 nm (Fig. 3c). This thickness was estimated since the material had to be coated with a gold layer so that the measurement could be taken. The thickness of the CMO thin film heat-treated in the RF could not be measured because the structure was too thin. The grain size of the CMO thin films was around 80 nm. The surface micrographs of the crystalline films presented homogeneous and crack-free morphologies (Fig. 3d).

Fig. 4 presents reflectivity spectra of the CMO thin films obtained between 200 and 800 nm. All the CMO thin films showed two bands, one between 278 and 287 nm (4.5 and 4.3 eV) and the other around 368 nm (3.4 eV). The band around 282 nm (4.4 eV) was attributed to electronic transitions within the MoO_4^{2-} complex, according to Spassky et al. [41] and Marques et al. [4]. The peak observed at 368 nm (3.4 eV) corresponded to the creation of the excitonic state in Ca^{2+} [4,41].

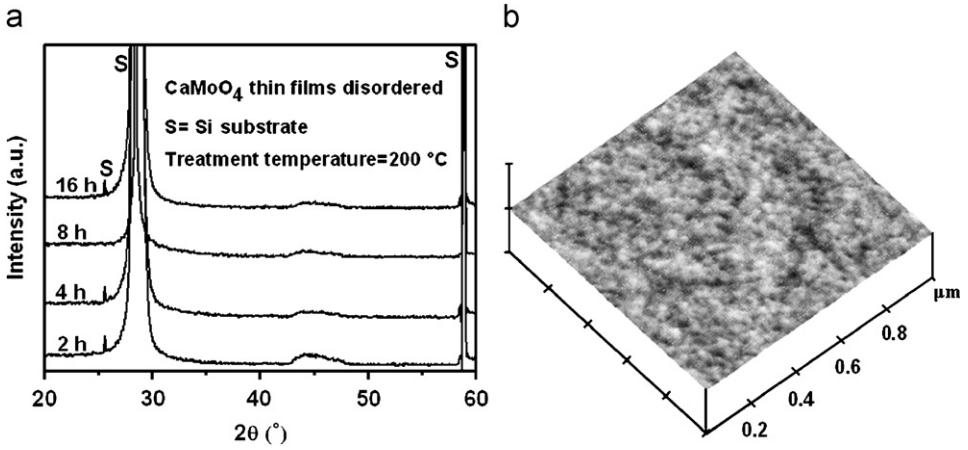

Fig. 2. Disordered $CaMoO_4$ thin films deposited in Si(100) and heat-treated at 200 °C: (a) X-ray diffraction patterns of thin films heat treated for 2, 4, 8 and 16 h and (b) AFM 3D image for the surface of $CaMoO_4$ thin films heat-treatment at 200 °C for 2 h.

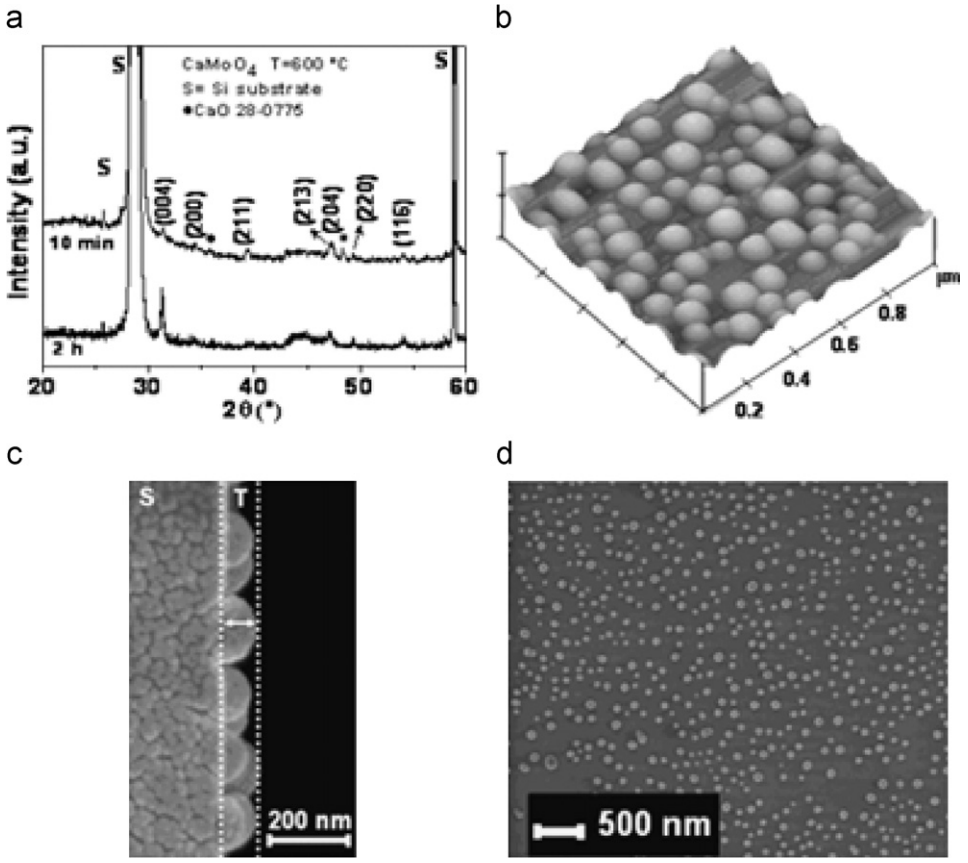

Fig. 3. Ordered $CaMoO_4$ thin films deposited in Si(100) and heat-treated at 600 °C: (a) X-ray diffraction patterns of thin films heat treated for 10 min and 2 h, (b) AFM 3D images for the surfaces of thin films heat treated for 2 h in a resistive furnace, (c) HR-SEM micrograph of thickness and (d) of surface thin films heat treated in a microwave for 10 min, where S = substrate and T = thickness.

The band gap (E_g) was estimated by plotting $(\alpha h\nu)^2$ as a function of $(h\nu - E_g)$. The optical absorption coefficient, α, can be obtained by $\alpha = [1/d*(\ln(1/T))]$, where d is the film's estimated thickness and T is the transmittance [42]. The α values we obtained for our thin films were higher than 10^4; according to Sian and Reddy [43], optical absorption coefficient α values exceeding 10^4 confirm the existence of direct band gaps. Zhang et al. [44] showed that the valence and conduction bands (CBs) near the band gap are dominated by molecular orbitals associated with the $MoO_4^{-\alpha}$ ions, where $\alpha \approx 2$, and also that CMO have direct band gaps. Based on our experimental data, the E_g values calculated for CMO thin films varied from 4.28 and 4.86 eV (see Table 2).

The decrease in the band gap in structurally disordered thin films can be attributed to oxygen vacancies, lattice defects, impurities and/or local bond distortions, which yield localized electronic levels in the band gap of this material. However, the tail observed in the disordered samples indicated only the presence of defects and, hence, of localized electronic levels in the forbidden band gap, without indicating the nature of these defects.

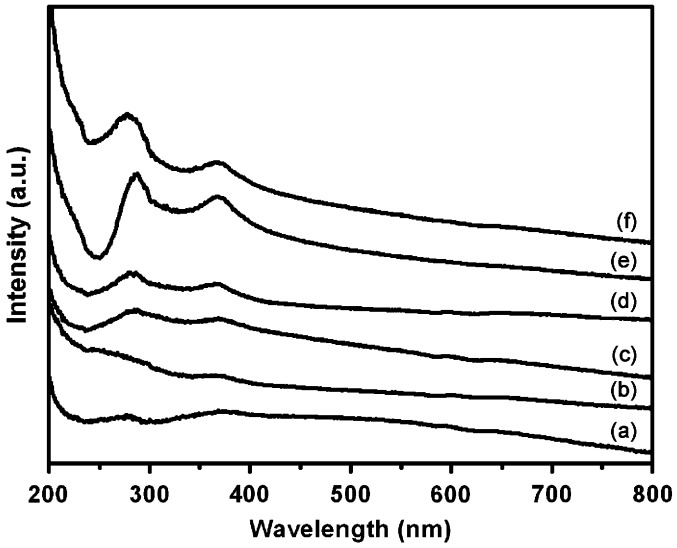

Fig. 4. Reflectivity spectra recorded in the 200–800 nm range of $CaMoO_4$ thin films heat-treated at 200 °C for 2 h (a), 4 h (b), 8 h (c) and 16 h (d), at 600 °C for 2 h (e) in a resistive furnace and heat-treated at 600 °C in a microwave for 10 min (f).

Table 2
E_g data of $CaMoO_4$ thin films

Samples	E_g (eV)
$CaMoO_4$—200 °C/2 h	4.28
$CaMoO_4$—200 °C/8 h	4.71
$CaMoO_4$—200 °C/16 h	4.80
$CaMoO_4$—600 °C/2 h (furnace)	4.81
$CaMoO_4$—600 °C/10 min (microwave)	4.86

Oxygen vacancies in molybdenum occur in three different charge states: the $[MoO_3 \cdot V_O^X]$ complex state, which presents two paired electrons $\underline{\uparrow\downarrow}$ and is neutral relative to the lattice, the singly ionized $[MoO_3 \cdot \overline{V_O^{\cdot}}]$ complex state, which has one unpaired electron $\underline{\uparrow}$, and the $[MoO_3 \cdot V_O^{\cdot\cdot}]$ complex state, which does not trap any electrons and is doubly positively charged in relation to the lattice. We speculate that these oxygen vacancies induce new energy in the band gap and can be attributed to the molybdenum–oxygen complex vacancy centers.

In order to model the presence of complex clusters and their relation to new energy in the band gap, a detailed theoretical study was made of the band structure and atom-resolved projected DOS in ordered CMO-o, and disordered CMO-d_1, CMO-d_2, CMO-d_3 models.

Fig. 5a reports the calculated band structure of bulk CMO-o. The top of the valence band (VB) and the bottom of the CB are at the Γ point. The minimal direct gap is 5.15 eV, very close to the experimental one deduced from the optical absorption edge, which we found to be 4.86–4.81 eV for the thin film annealed at 600 °C for 10 min and 2 h, respectively (see Table 2).

The calculated band structure of bulk CMO-d_1 is depicted in Fig. 5b. The direct minimal gap in Γ is 4.83 eV and can be compared with the thin film annealed for 16 h (4.80 eV).

The calculated band structures of CMO-d_2 and CMO-d_3 are depicted in Figs. 5c and d, respectively. The direct minimal gap in Γ is 4.45 eV for the CMO-d_2 model and 3.98 eV for the CMO-d_3 model. The direct gap of the dislocated models CMO-d_2 and CMO-d_3 can be compared with the optical gap of the disordered structures annealed for 8 h (4.71 eV) and 2 h (4.28 eV), respectively.

The molybdenum, which is the lattice former, ideally tends to bond with four oxygen atoms, but before it reaches this ideal configuration there are various coordination numbers for Mo in the structure. Before it becomes crystallized, the structure is a mixture of MoO_x complex clusters (x = mostly 3 and 4) intercalated with Ca atoms. The higher the annealing temperature, the more frequent the $[MoO_4]$ complex and the more structurally ordered the structure. These results show that our data are consistent with the interpretation that the exponential optical absorption edge and the optical band gap are controlled by the degree of structural disorder in the lattice of the CMO thin film.

For the CMO-o (Fig. 5a), the VBs are derived from O ($2p_x$, $2p_y$, $2p_z$) atomic orbitals. These bands are separated by a direct gap from the first CB, which derives from transition-metal molybdenum ($4d_{xy}$, $4d_{xz}$, $4d_{yz}$) atomic orbitals, designated as "t_{2g}" by comparison with the $[WO_4]$ regular cluster. Above these six bands come four Ti ($4d_{z2-y2}$ and $4d_{z2}$) character bands called "e_g". For the dislocated models (CMO-d_1, CMO-d_2 and CMO-d_3), although the VB is globally constituted of O ($2p_x$, $2p_y$, $2p_z$) character states, the top depends mainly on the oxygen O9 which has lost its connection with the Mo2 that was dislocated. The CB is composed of the 4d states of Mo2 which was dislocated in an apparently random splitting of bands (Fig. 5b–d).

The calculated total and atom-resolved projected DOS of CMO-o, CMO-d_1, CMO-d_2 and CMO-d_3 are shown in Fig. 6, ranging from −6 eV below the top of the VB to 9 eV above. In the case of CMO-o, the upper VB consists predominately of the O (2p) states, distributed equally in the axial oxygens of the structure (Fig. 6a). In the case of CMO-d_1 (Fig. 6b), although the VB also consists of O (2p) states, the upper part, i.e., the new states, present a slightly prevalent O9 (2p) character, the oxygen atom that loses its connection with Mo2. In the case of CMO-d_2 (Fig. 6c), the upper VB consists mainly of the 2p oxygen states of O9. The upper VB of the CMO-d_3 structure consists almost entirely of the 2p oxygen states of O9. These results indicate that a disorder in the network former creates a lift of degeneracy in the forbidden band gap when compared with the CMO-o model. The CB clearly consists of the Mo (4d) states in the ordered model. The disordered structures consist mainly of the 4d molybdenum state of Mo2 which was dislocated. The Mo–O covalent bond creates a limited Mo (4d) contribution in the O (2p) region, as well as a weak O (2p) contribution to the Mo (4d) area.

The Ca (4s) states (not shown) are found in energies above −6 eV and are more dispersed in disordered models. These levels are weakly hybridized with oxygen levels in the CMO-d models.

Fig. 7a illustrates PL spectra recorded at room temperature for the CMO thin films annealed at 200 or 600 °C for different periods of time and excited by the 488 nm line of an argon ion laser. The profile of the emission band is typical of a multiphonon process, i.e., a system in which relaxation occurs by several paths, involving the participation of numerous states within the band gap of the material. This behavior is associated with the structural disorder of CMO and indicates the presence of additional electronic levels in the forbidden band gap of the material.

The general aspect of the spectrum is a broad band covering a large part of the visible spectrum from ~470 to 820 nm. The bands are broad and intense, particularly in the case of the disordered thin film annealed at 200 °C for 2 h and centered at 578 nm (2.14 eV). The intensity of disordered thin films annealed at 200 °C for the subsequent annealing times decreases. The PL emission of structural ordered thin films annealed at 600 °C in the RF showed a very low emission, while the PL emission of the films annealed in the MW oven at 600 °C practically disappeared.

The strength of the electron–phonon interaction can be indicated by the difference between the excitation and the emission maximum (Stokes shift). As can be seen, the Stokes

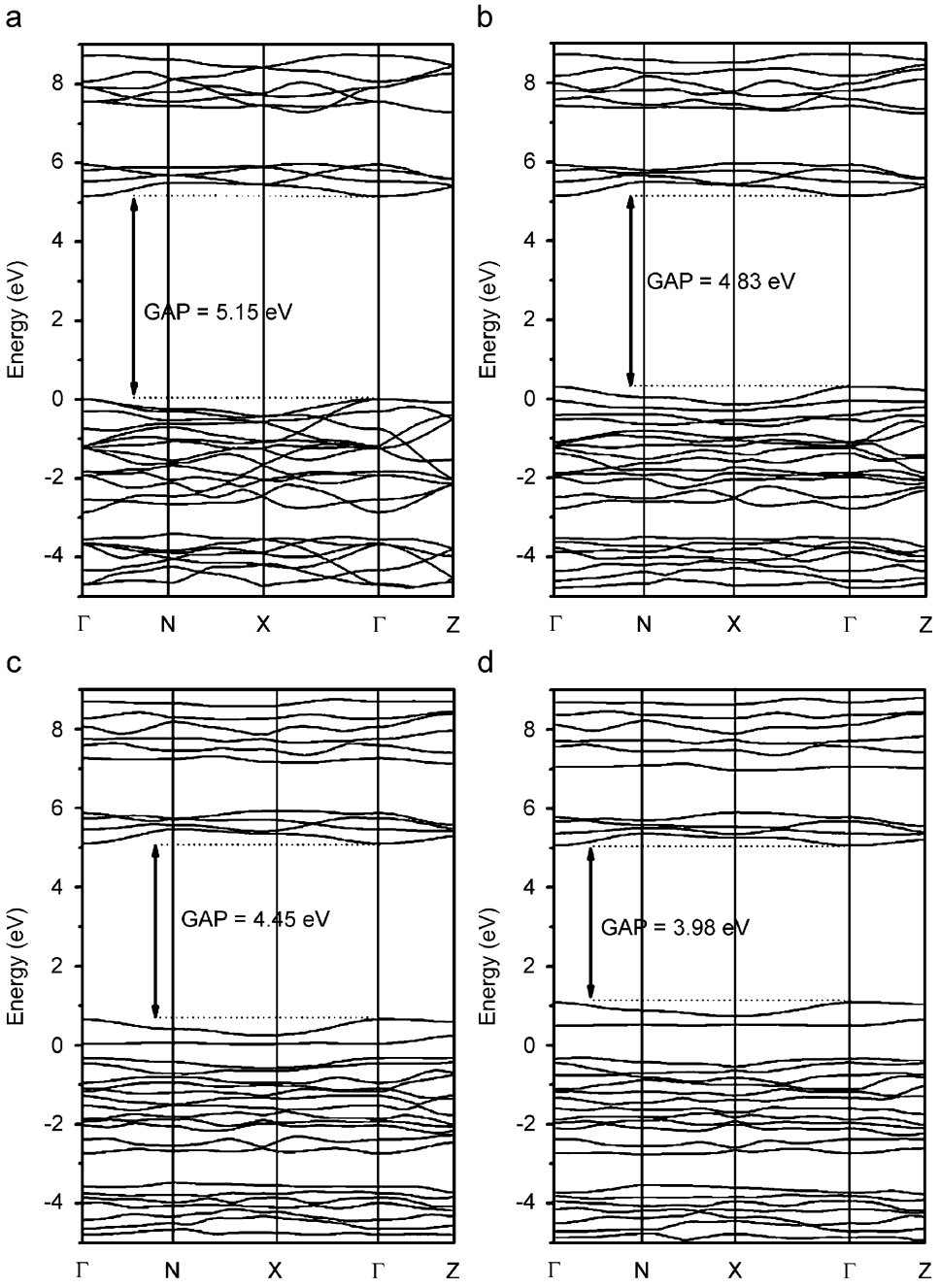

Fig. 5. The calculated band structure of bulk CMO-o (a), CMO-d_{01} (b), CMO-d_{02} (c) and CMO-d_{03} (d).

shift declined gradually in the disordered thin films annealed at 200 °C as the annealing temperatures increased, but the decline was considerable in the ordered films annealed at 600 °C. This indicates a dependence on electron–phonon interaction and the degree of disorder in the lattice. This rearrangement of the lattice in disordered thin films annealed at 200 °C for 2–16 h is not detected by a long-range measurement such as XRD (Fig. 2a). However, the UV and PL experimental measurements and the *ab initio* theoretical calculation indicate that significant changes in the gap states occurred as the system became ordered (Fig. 4–7).

We believe that the PL curves shown in Fig. 7 consist of five PL components, herein called blue-green component (maximum below 508.5 nm), green component (maximum below 537 nm), yellow component (maximum below 575 nm), orange component (maximum below 613 nm), and red component (maximum below 669 nm), in reference to the region where the components' maxima appear. In this context, to better understand the PL properties and their dependence on the structural order–disorder of the lattice, the PL curves were analyzed using the deconvolution program PickFit [45]. Based on the Gaussian line broadening mechanism for luminescence processes, the fine features in the PL spectra of samples were deconvoluted. The features extracted from the deconvolution curves and from the area under the curve of the respective transitions are listed in Table 3 and shown in Fig. 7b–f. As can be seen in this figure, increasing the annealing temperature and time caused the structure of the CMO thin films to become more ordered, favoring the emission of green light (smaller wavelength) with higher energies.

Each color represents a different type of electronic transition and is linked to a specific structural arrangement. The yellow,

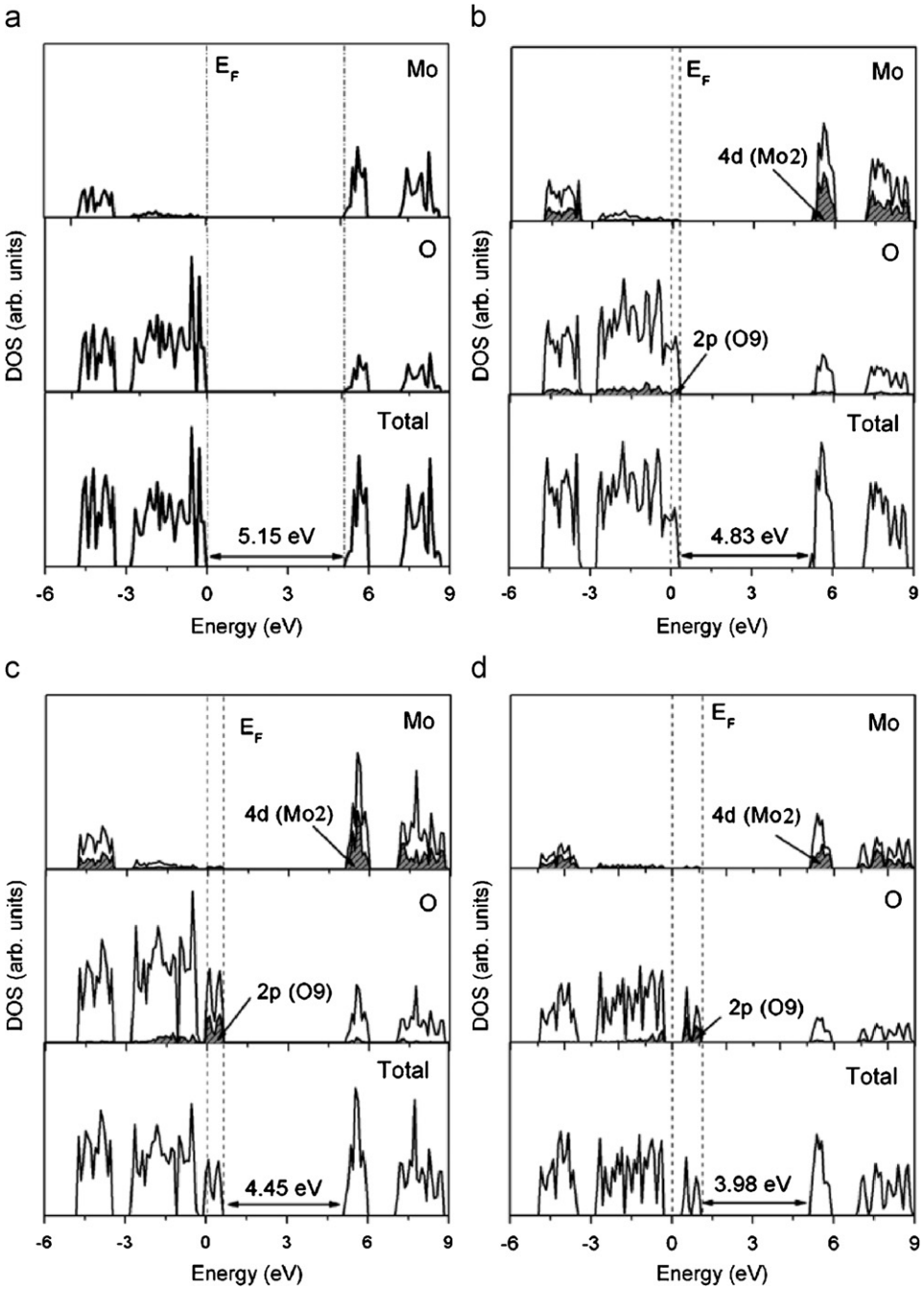

Fig. 6. Projected DOS of CMO-o (a), CMO-d_{01} (b), CMO-d_{02} (c) and CMO-d_{03} (d).

orange and red peaks diminish and the green peak expands with the heat treatment, since yellow-orange-red emission is linked to the disordered structure and green emission is connected to the ordered structure.

The literature offers many valid hypotheses to explain all the possible mechanisms that occur during the photon excitation and decay process [24,26].

First principles quantum mechanical calculations have shown that the break in symmetry creates inherent defects in the lattice and is responsible for the presence of electronic states in the band gap.

In our model, the Wild Band Model [46], the most important events occur before excitation, i.e., before the photon arrives. The short and intermediate range structural defects generate localized states in the band gap and inhomogeneous charge distribution in the cell, thus allowing for trapping of electrons. The localized levels are energetically distributed, so that various energies are able to excite the trapped electrons.

Before donor excitation, a hole in the acceptor and an electron in a donor are created according to the following equations, where Kröger–Vink notation is used for complex clusters:

$$[MoO_4]^x + [MoO_3 \cdot V_O^x] \rightarrow [MoO_4]' + [MoO_3 \cdot V_O^{\bullet}], \quad (1)$$

$$[MoO_4]^x + [MoO_3 \cdot V_O^{\bullet}] \rightarrow [MoO_4]' + [MoO_3 \cdot V_O^{\bullet\bullet}], \quad (2)$$

where $[MoO_4]'$ are donors and $[MoO_3 \cdot V_O]$ are donors/acceptors and $[MoO_3 \cdot V_O^{\cdot}]$ are acceptors.

In the complex, the $[MoO_4]'$ clusters act as electrons donors, while the vacancy complex $[MoO_3 \cdot V_O]$ tends to trap electrons and/or holes and $[MoO_3 \cdot V_O^{\cdot}]$ acts as electron traps. These equations

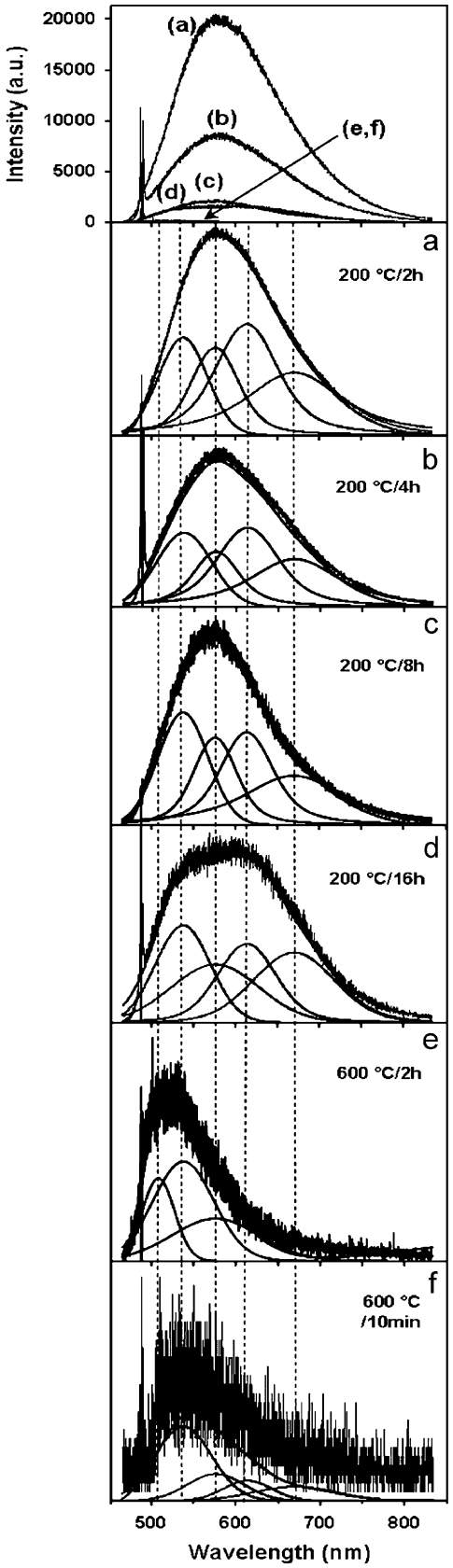

Fig. 7. Room-temperature PL spectra of $CaMoO_4$ thin films excited with the 488 nm line of an argon ion laser heat-treated at 200 °C for 2 h (a), 4 h (b), 8 h (c) and 16 h (d), at 600 °C for 2 h (e) and at 600 °C for 10 min (f) and yours respectively components of PL in blue-green, green, yellow, orange and red region.

Table 3
The fitting parameters of the Gaussian peaks for PL obtained with excitation wavelength at 488 nm

T (°C)	BGC (%)[a]	GC (%)[a]	YC (%)[a]	OC (%)[a]	RC (%)[a]
200_2 h	0	18	19	32	31
200_4 h	0	21	17	32	30
200_8 h	0	24	20	26	30
200_16 h	0	25	24	24	28
600_2 h	21	49	30	0	0
600_10 min	0	54	19	12	15

T = temperature of heat annealing; BGC = blue-green component of PL; GC = green component of PL; YC = yellow component of PL; OC = orange component of PL; and RC = red component of PL.

[a] Obtained by dividing the area of each decomposed PL curves by the total PL area.

suggest that the oxygen vacancy-trapped electron in the VB is a necessary requirement for the transition of a valence-band hole in the CB. This means that most of the electrons around oxygen vacancies are released and, therefore, such oxygen vacancy complex sites are relatively positively charged. Moreover, oxygen vacancies tend to trap photogenerated electrons. The charge transfer occurring as proposed in Eqs. (1) and (2) creates electrons and hole polarons that can be designed as bipolarons. After photon excitation, the recombination and decay process follows the many valid hypotheses proposed in the literature [24,26].

The present work shows that these complex clusters already existing in the ground state facilitate the emission process, leading to PL, i.e., to radiative recombination. Ordered–disordered CMO powders thus intrinsically possess the necessary condition for creating PL at room temperature.

4. Conclusions

CMO thin films were produced by a simple synthesis method. The CMO scheelite-type crystalline phase was identified at 600 °C. HRSEM and AFM micrographs revealed a tendency for the grain boundaries to become well defined with increasing treatment temperature and time.

First principles quantum mechanical calculations showed that breaks in symmetry create inherent defects in the lattice and are responsible for the presence of electronic states in the band gap. These inherent defects are linked to structural disorder already existing in the ground state, which facilitates the emission process and leads to PL, i.e., radioactive recombination. In our model, the Wild Band Model, the most important events occur before excitation, i.e., before the photon arrives. The oxygen complex clusters generate an inhomogeneous charge distribution in the cell, thus allowing the trapping of electrons. The localized levels are energetically distributed, so that various energies are able to excite the trapped electrons.

The optical properties suggest that this material is a highly promising candidate for PL applications. Processing thin films in such a manner does not require expensive equipment or reagents, deposition in high vacuum chambers or special atmospheric control, and has the added advantage of requiring lower temperatures, less time and lower costs.

Acknowledgments

The authors gratefully acknowledge the financial support granted by the Brazilian research funding agencies CEPID, CNPq and PRONEX.

References

[1] N. Klassen, S. Shmurak, B. Red'kin, B. Ille, M. Lebeau, P. Lecoq, M. Schneegans, Nucl. Instrum. Methods A 486 (1–2) (2002) 431.
[2] F.A. Danevich, A.S. Georgadze, V.V. Kobychev, B.N. Kropivyansky, V.N. Kuts, A.S. Nikolaiko, V.I. Tretyak, Y. Zdesenko, Phys. Lett. B 344 (1–4) (1995) 72.
[3] W.S. Cho, M. Yashima, M. Kakihana, A. Kudo, T. Sakata, M. Yoshimura, J. Am. Ceram. Soc. 80 (3) (1997) 765.
[4] A.P.A. Marques, D.M.A. de Melo, E. Longo, C.A. Paskocimas, P.S. Pizani, E.R. Leite, J. Solid State Chem. 178 (7) (2005) 2346.
[5] A.P.A. Marques, D.M.A. Melo, C.A. Paskocimas, P.S. Pizani, M.R. Joya, E.R. Leite, E. Longo, J. Solid State Chem. 179 (2006) 658.
[6] L. Chen, Y. Gao, Chem. Eng. J. 131 (2007) 181.
[7] C.T. Xia, V.M. Fuenzalida, J. Eur. Ceram. Soc. 23 (3) (2003) 519.
[8] P. Yang, G.Q. Yao, J.H. Lin, Inorg. Chem. Commun. 7 (3) (2004) 389.
[9] V.B. Mikhailik, H. Kraus, D. Wahl, M.S. Mykhaylyk, Phys. Status Solidi B 242 (2) (2005) R17.
[10] Y.S. Hu, W.D. Zhuang, H.Q. Ye, J. Rare Earths 22 (6) (2004) 821.
[11] P. Yu, J. Bi, D.Q. Xiao, L.P. Chen, X.L. Jin, Z.N. Yang, J. Electroceram. 16 (4) (2006) 473.
[12] C.T. Xia, V.M. Fuenzalida, R.A. Zarate, J. Alloys Compd. 316 (1–2) (2001) 250.
[13] M.A.M.A. Maurera, A.G. Souza, L.E.B. Soledade, F.M. Pontes, E. Longo, E.R. Leite, J.A. Varela, Mater. Lett. 58 (5) (2004) 727.
[14] J.A. Groenink, G. Blasse, J. Solid State Chem. 32 (1) (1980) 9.
[15] A.A. Annenkov, M.V. Korzhik, P. Lecoq, Nucl. Instrum. Methods A 490 (1–2) (2002) 30.
[16] P. Lecoq, I. Dafinei, E. Auffray, M. Schneegans, M.V. Korzhik, O.V. Missevitch, V.B. Pavlenko, A.A. Fedorov, A.N. Annenkov, V.L. Kostylev, V.D. Ligun, Nucl. Instrum. Methods A 365 (2–3) (1995) 291.
[17] M.V. Korzhik, V.B. Pavlenko, T.N. Timoschenko, V.A. Katchanov, A.V. Singovskii, A.N. Annenkov, V.A. Ligun, I.M. Solskii, J.P. Peigneux, Phys. Status Solidi A 154 (2) (1996) 779.
[18] E.V. Sokolenko, V.M. Zhukovskii, E.S. Buyanova, Y.A. Krasnobaev, Inorg. Mater. 34 (5) (1998) 499.
[19] B.M. Sinelnikov, E.V. Sokolenko, V.Y. Zvekov, Inorg. Mater. 32 (9) (1996) 999.
[20] T.L. Chen, X.M. Li, K.S. Wan, W.L. Zhu, G. Pezzotti, Appl. Phys. Lett. 87 (18) (2005) 181914.
[21] S. Myhajlenko, A. Bell, F. Ponce, J.L. Edwards, Y. Wei, B. Craigo, D. Convey, H. Li, R. Liu, J. Kulik, J. Appl. Phys. 97 (1) (2005) 014101.
[22] T. Hara, Mater. Chem. Phys. 91 (2–3) (2005) 243.
[23] Y.H. Chen, C.S. Shi, G.Q. Hu, J. Appl. Phys. 87 (3) (2000) 1503.
[24] R. Leonelli, J.L. Brebner, Solid State Commun. 54 (6) (1985) 505.
[25] R. Leonelli, J.L. Brebner, Phys. Rev. B 33 (12) (1986) 8649.
[26] R.I. Eglitis, E.A. Kotomin, G. Borstel, Eur. Phys. J. B 27 (4) (2002) 483.
[27] R.I. Eglitis, E.A. Kotomin, V.A. Trepakov, S.E. Kapphan, G. Borstel, J. Phys.: Condens. Matter 14 (39) (2002) L647.
[28] M. Anicete-Santos, F.C. Picon, M.T. Escote, E.R. Leite, P.S. Pizani, J.A. Varela, E. Longo, Appl. Phys. Lett. 88 (21) (2006) 211913.
[29] V.M. Longo, E. Orhan, L.S. Cavalcante, S.L. Porto, J.W.M. Espinosa, J.A. Varela, E. Longo, Chem. Phys. 334 (2007) 180.
[30] F.M. Pontes, E. Longo, E.R. Leite, E.J.H. Lee, J.A. Varela, P.S. Pizani, C.E.M. Campos, F. Lanciotti, V. Mastelaro, C.D. Pinheiro, Mater. Chem. Phys. 77 (2) (2003) 598.
[31] V.R. Saunders, R. Dovesi, C. Roetti, M. Causa, N.M. Harrison, R. Orlando, C.M. Zicovich-Wilson, CRISTAL98 User's Manual, University of Torino, Torino, 2003.
[32] C.T. Lee, W.T. Yang, R.G. Parr, Phys. Rev. B 37 (2) (1988) 785.
[33] A.D. Becke, J. Chem. Phys. 98 (7) (1993) 5648.
[34] J. Muscat, A. Wander, N.M. Harrison, Chem. Phys. Lett. 342 (3–4) (2001) 397.
[35] 〈http://www.tcm.phy.cam.ac.uk/~mdt26/basis_sets/Mo_basis.txt〉.
[36] 〈http://www.crystal.unito.it〉.
[37] A. Kokalj, J. Mol. Graph. 17 (1999) 176.
[38] JCPDS No. 29-0351.
[39] JCPDS No. 08-0482.
[40] K. Nakamoto, Infrared and Raman Spectra of Inorganic and Coordination Compounds, Wiley, New York, 1986.
[41] D.A. Spassky, S.N. Ivanov, V.N. Kolobanov, V.V. Mikhailin, V.N. Zemskov, B.I. Zadneprovski, L.I. Potkin, Radiat. Meas. 38 (4–6) (2004) 607.
[42] M. Sreemany, S. Sen, Mater. Chem. Phys. 83 (1) (2004) 169.
[43] T.S. Sian, G.B. Reddy, Sol. Energy Mater. Sol. Cells 82 (3) (2004) 375.
[44] Y. Zhang, N.A.W. Holzwarth, R.T. Williams, Phys. Rev. B 57 (20) (1998) 12738.
[45] T. Ding, W.T. Zheng, H.W. Tian, J.F. Zang, Z.D. Zhao, S.S. Yu, X.T. Li, F.L. Meng, Y.M. Wang, X.G. Kong, Solid State Commun. 132 (12) (2004) 815.
[46] V.M. Longo, L.S. Cavalcante, A.T. de Figueiredo, L.P.S. Santos, E. Longo, J.A. Varela, J.R. Sambrano, C.A. Paskocimas, F.S. De Vicente, A.C. Hernandes, Appl. Phys. Lett. 90 (9) (2007) 091906.